Nanoscale

PAPER

View Article Online
View Journal | View Issue

Cite this: *Nanoscale*, 2015, **7**, 5203

Porous metallic MoO_2-supported MoS_2 nanosheets for enhanced electrocatalytic activity in the hydrogen evolution reaction†

Linjing Yang,[a] Weijia Zhou,*[a] Dongman Hou,[b] Kai Zhou,[a] Guoqiang Li,[b] Zhenghua Tang,[a] Ligui Li[a] and Shaowei Chen*[a,c]

Received 14th November 2014,
Accepted 9th February 2015

DOI: 10.1039/c4nr06754a

www.rsc.org/nanoscale

Advanced materials for electrocatalytic water splitting are central to renewable energy research. In this work, MoS_2 nanosheets supported on porous metallic MoO_2 (MoS_2/MoO_2) were produced by sulfuration treatments of porous and highly conductive MoO_2 for the hydrogen evolution reaction. Porous MoO_2 with one-dimensional channel-like structures was prepared by calcination at elevated temperatures using phosphomolybdic acid as the precursor and mesoporous silica (SBA-15) as the template, and the subsequent hydrothermal treatment in the presence of thioacetamide led to the transformation of the top layers to MoS_2 forming MoS_2/MoO_2 composites. Electrochemical studies showed that the obtained composites exhibited excellent electrocatalytic activity for HER with an onset potential of −104 mV (*vs.* RHE), a large current density (10 mA cm^{-2} at −0.24 V), a small Tafel slope of 76.1 mV dec^{-1} and robust electrochemical durability. The performance might be ascribed to the high electrical conductivity and porous structures of MoO_2 with one-dimensional channels of 3 to 4 nm in diameter that allowed for fast charge transport and collection.

Introduction

As a clean chemical fuel with a high-energy density, hydrogen has been hailed as a promising alternative and renewable energy source that may replace fossil fuels in the future. Accordingly, hydrogen produced by environmentally friendly electrochemical water splitting has recently been emerging as a key technology component of hydrogen economy.[1–4] In these studies, advanced catalysts for the hydrogen evolution reaction (HER) are generally needed to reduce overpotential and increase the catalytic current density.[5–11] Pt-group metals are the most active catalysts for HER and can dramatically enhance the reaction rate with almost no overpotential for high efficiency energy conversion.[12] However, their scarcity and high costs have inhibited large scale applications in electrochemical water splitting. Therefore, extensive research efforts have been devoted to the development of non-platinum electrocatalysts for HER. For instance, Hinnemann *et al.*[13] reported in 2005 that MoS_2 nanoparticles exhibited an apparent electrocatalytic activity for HER, which was predicted to be comparable to that of Pt. The interest in using MoS_2 as water splitting electrocatalysts has since been intensified, with a focus on the enhancement of the material catalytic properties by, for instance, loading catalysts on conductive substrates (*e.g.*, graphene-protected 3D Ni foams, graphene nanosheets, and porous Au),[14–17] doping treatment (*e.g.* MoO_2/N-doped MoS_2 and oxygen incorporated MoS_2),[18,19] and enhanced exposure of active edges.[20–22] Among these, Chang *et al.*[14] deposited graphene layers on the surface of 3D Ni foams and used them as a conducting solid support for MoS_x. The hydrogen evolution rate was found to reach 302 mL g^{-1} cm^{-2} h^{-1} at an overpotential of −200 mV, where the Ni foams-supported graphene sheets served as a robust scaffold and increased the stability of the catalysts in acid. In another study, Ge *et al.*[15] reported a new type of nanoporous electrocatalysts by chemically plating a thin layer of amorphous molybdenum sulfide on the internal surface of de-alloyed nanoporous gold. The resulting $MoS_{2.7}$@Au electrode exhibits a 6-fold higher catalytic activity than conventional molybdenum sulfide catalysts in 0.5 M H_2SO_4 solution with a Tafel slope of 41 mV dec^{-1}. The improved catalytic performance was mainly due to the highly conductive and large-surface nanoporous gold. However,

[a]*New Energy Research Institute, College of Environment and Energy, South China University of Technology, Guangzhou Higher Education Mega Center, Guangzhou, Guangdong 510006, China. E-mail: eszhouwj@scut.edu.cn*
[b]*School of Materials Science and Engineering, South China University of Technology, Tianhe District, Guangzhou, Guangdong 510641, China*
[c]*Department of Chemistry and Biochemistry, University of California, 1156 High Street, Santa Cruz, California 95064, USA. E-mail: shaowei@ucsc.edu*
†Electronic supplementary information (ESI) available: XRD patterns, Raman spectra, TEM images and additional voltammetric data. See DOI: 10.1039/c4nr06754a

porous Au is expensive. Is it possible to find low-cost porous conductive substrates for the synthesis of high-performance HER catalysts? This is the primary motivation of the present study which is focused on MoS_2 nanosheets grown on highly conductive porous MoO_2.

Molybdenum dioxide (MoO_2) with a distorted rutile structure is an unusual and attractive transition metal oxide because of its low metallic electrical resistivity (8.8×10^{-5} Ω cm at 300 K in bulk samples), high melting point, and high chemical stability.[21] Mesoporous crystalline MoO_2 materials have been prepared as potential electrode materials in Li ion batteries.[23,24] Herein, porous MoO_2 were synthesized by calcination at elevated temperatures using phosphomolybdic acid as a precursor and porous silica SBA-15 as a hard template, which exhibited high electrical conductivity and a large surface area. The subsequent sulfuration treatment led to the transformation of the top layers into MoS_2 nanosheets. The structures of the resulting MoS_2/MoO_2 nanocomposites were then characterized by various microscopic and spectroscopic measurements. Electrochemical measurements showed that the MoS_2/MoO_2 nanocomposites exhibited an apparent HER activity with a low overpotential of −104 mV and robust electrochemical durability.

Experimental section

Synthesis of porous metallic MoO_2

Mesoporous silica SBA-15 and porous metallic MoO_2 were prepared by the following literature procedures.[24,25] In a typical experiment, SBA-15 (1.0 g) was mixed with phosphomolybdic acid ($H_3PMo_{12}O_{40}$, 4.2 g) in ethanol (15 mL) at room temperature under stirring in an open crucible. After the evaporation of ethanol, yellow powders were obtained and loaded on a quartz boat and heated to 500 °C in a tube furnace at a heating rate of 2 °C min^{-1} under an atmosphere of 10% H_2 and 90% Ar. The heating was maintained at this temperature for 5 h. The obtained MoO_2/SBA-15 composite was treated by 60 mL of a 4% HF aqueous solution to remove the silica template, affording porous MoO_2.

Synthesis of MoS_2 nanosheets supported on porous metallic MoO_2 (MoS_2/MoO_2)

MoS_2 nanosheets supported on mesoporous metallic MoO_2 were prepared by a simple hydrothermal process. In a typical experiment, 50 mg of porous MoO_2 obtained above and 150 mg of thioacetamide (TAA) were dissolved in 40 mL of water. The solution was then transferred to a 50 mL Teflon-lined stainless steel autoclave and heated in an electric oven at 200 °C for 6 h, 12 h, 24 h or 48 h. The autoclave was naturally cooled to room temperature and the obtained MoS_2/MoO_2 composites were washed with distilled water, and dried at 80 °C for 12 h, which were denoted as MoS_2/MoO_{2-x} (x = 6 h, 12 h, 24 h or 48 h).

For comparison, pure MoS_2 nanosheets were also prepared in a similar way but without the MoO_2 scaffold. Experimentally, 30 mg of sodium molybdate ($Na_2MoO_4{\cdot}2H_2O$) and 60 mg of thioacetamide (C_2H_5NS) were dissolved in 20 mL of deionized water to form a transparent solution. The solution was transferred to a Teflon-lined stainless steel autoclave and then heated in an electric oven at 200 °C for 24 h. Pure MoS_2 nanosheets, as a black product, were harvested after the solution was centrifuged and then dried at 50 °C for 12 h.

Characterizations

Field-emission scanning electron microscopic (FESEM, Model JSM-7600F) measurements were employed to characterize the morphologies of the obtained samples. Transmission electron microscopic (TEM) measurements were carried out using a JOEL JEM 2100F microscope. Powder X-ray diffraction (XRD) and small-angle XRD patterns of the samples were recorded using a Bruke D8 Advance powder X-ray diffractometer with Cu Kα (λ = 0.15406 nm) radiation. X-ray photoelectron spectroscopic (XPS) measurements were performed using an ESCALAB 250. Raman spectra were recorded using a RENISHAW inVia instrument with an Ar laser source of 488 nm in a macroscopic configuration. The BET surface area was characterized by using Micromeritics ASAP 2010 with nitrogen adsorption at 77 K and the Barrett–Joyner–Halenda (BJH) method.

Electrochemistry

Electrochemical measurements were performed with an electrochemical workstation (Solartron Analytical 1287 + 1260) in 0.5 M H_2SO_4 aqueous solution. A saturated calomel electrode ($Hg/HgCl_2$ in saturated KCl) and a platinum wire were used as the reference electrode and the counter electrode, respectively. A calculated amount of MoS_2, MoO_2, or MoS_2/MoO_2 was loaded on a glassy carbon electrode which was used as the working electrode. Experimentally, 4 mg of the respective catalyst powders was dispersed in 1 mL of 4 : 1 (v/v) water–ethanol mixed solvents with 40 μL of a Nafion solution under ultrasonication for 30 min. A 4 μL of the resulting solution was drop cast onto the glassy-carbon disk using a microliter syringe and dried at room temperature. The catalyst loadings were all 0.22 mg cm^{-2}.

Polarization curves were acquired by sweeping the potential from 0 to −0.8 V (*vs.* SCE) at a potential sweep rate of 5 mV s^{-1}, with ohmic losses compensated electronically.[26] The accelerated stability tests were performed in 0.5 M H_2SO_4 at room temperature by potential cycling between +0.1 and −0.5 V (*vs.* SCE) at a sweep rate of 100 mV s^{-1} for a given number of cycles. Current–time responses were monitored by chronoamperometric measurements for up to 10 h. Hydrogen production at the MoS_2/MoO_2 modified glassy carbon electrode was carried out at −0.5 V (*vs.* SCE).

In all measurements, the SCE reference electrode was calibrated with respect to a reversible hydrogen electrode (RHE). The calibration was performed in a high-purity H_2 (99.999%) saturated electrolyte with two Pt wires as the working electrode and the counter electrode, respectively. Cyclic voltammograms (CVs) were acquired at a scan rate of 1 mV s^{-1}, and the average

of the two potentials at which the current crossed zero was taken as the thermodynamic potential for the hydrogen electrode reactions in 0.5 M H_2SO_4, $E_{SCE} = E_{RHE} + 0.273$ V.

Results and discussion

Fig. 1 describes the procedure for a typical synthesis of MoS_2/MoO_2 nanocomposites, which involves three major steps: (a) molecular sieves (SBA-15) were filled with phosphomolybdic acid, and then calcined under a 10% H_2/90% Ar atmosphere to synthesize MoO_2/SBA-15 by the decomposition of phosphomolybdic acid; (b) HF was used to remove the SBA-15 template and obtain one-dimensional porous MoO_2; (c) the hydrothermal reaction of porous MoO_2 with TAA led to the transformation of the top layers of MoO_2 into MoS_2 nanosheets forming MoS_2/MoO_2 composites.

The as-prepared samples were first characterized by using XRD measurements. From Fig. 2a, one can see that for the MoS_2/MoO_2-6 h sample (red curve), the main crystalline phase is MoO_2 (JCPDS: 32-0671, Monoclinic, a = 0.56 nm, b = 0.48 nm, c = 0.55 nm), with characteristic diffraction peaks at 26.0° (011), 31.8° (101), 36.9° (111), 41.5° (120), 53.3° (112), 60.2° (031) and 66.5° (131), which are all well-defined also with the MoO_2 sample (black curve). Several weak diffraction peaks

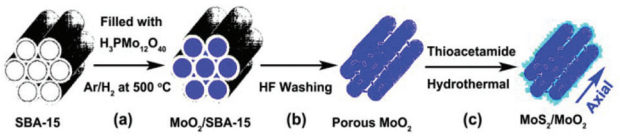

Fig. 1 Schematic of the synthesis of MoS_2 nanosheets supported on porous metallic MoO_2 (MoS_2/MoO_2).

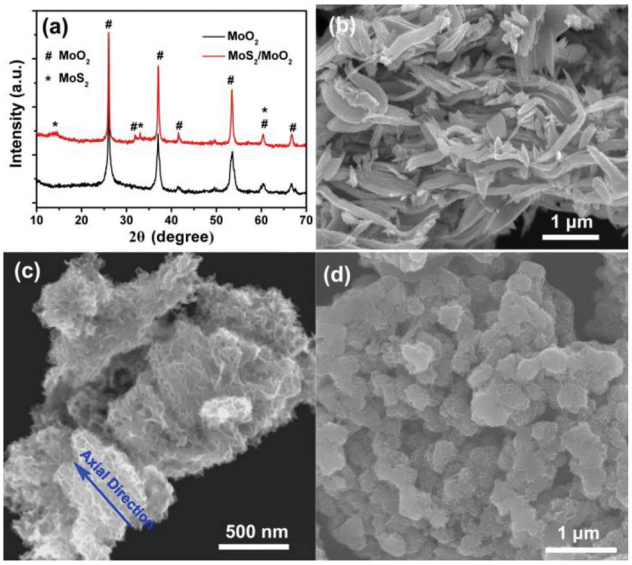

Fig. 2 (a) XRD of MoO_2 and MoS_2/MoO_2-6 h, (b) representative SEM image of MoO_2, (c) side-view and (d) top-view SEM images of MoS_2/MoO_2-6 h.

can also be seen at 14.5°, 33.0°, and 60.4° that are consistent with MoS_2 (003), (101), and (113) crystalline planes, respectively (JCPDS: 65-3656, hexagonal, $a = b$ = 0.32 nm, c = 1.8 nm). These results suggest the formation of MoO_2/MoS_2 composites. The XRD patterns of MoS_2/MoO_2 composites prepared for other hydrothermal reaction times (upto 48 h) are shown in Fig. S1.† It can be seen that in all samples, MoO_2 remained as the primary crystalline phase, along with weak diffraction peaks of MoS_2, suggesting that only the top layers of MoO_2 were chemically transformed into MoS_2 under hydrothermal conditions. The formation of MoS_2 was further confirmed by Raman spectroscopic measurements (Fig. S2†) which exhibited a series of vibrational bands at 120, 141.6, 192, 281, 333.4, and 374.2 cm^{-1} that are characteristic of MoS_2.[27] The MoO_2 vibrational bands are also well-defined at 817.3 and 990.7 cm^{-1}.[19,23,28]

SEM measurements were then carried out to examine the surface morphologies. Fig. 2b depicts an overview of the porous one-dimensional MoO_2 nanostructures with 200–300 nm in width and 1–3 μm in length, consistent with the dimensions of SBA-15 (Fig. S3†). After hydrothermal treatment with TAA for 6 h, it can be seen that the MoO_2 surfaces were decorated with a number of curvy nanosheets, as evidenced in SEM images in Fig. 2c (side view) and 2d (top view along the axial direction), which are most likely MoS_2 nanosheets. This is consistent with the XRD results. The mesoporous structure of the MoS_2/MoO_2-6 h composites was further confirmed by nitrogen adsorption/desorption measurements which featured a typical type-IV isotherm (Fig. S4†). However, because of the high molecular weight of MoO_2 and MoS_2, the MoS_2/MoO_2-6 h composites showed only a relatively low specific surface area of 34.58 $m^2\ g^{-1}$.

Mesostructures with regular spacing are well-defined in TEM measurements, as depicted in Fig. 3. From panel (a), it can be seen that the obtained porous MoO_2 displayed one-

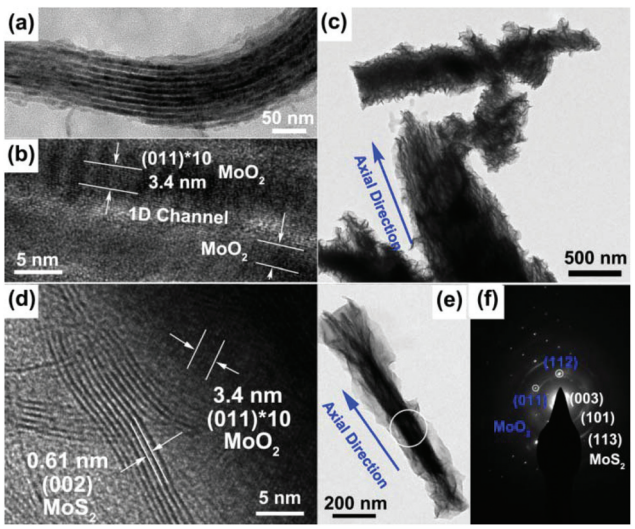

Fig. 3 TEM images of (a, b) porous MoO_2 and (c–e) MoS_2/MoO_2-6 h; (f) selected area electron diffraction patterns of MoS_2/MoO_2-6 h.

dimensional channels of 3 to 4 nm in diameter and 5 to 6 nm in wall thickness throughout the entire particle domain, indicating that the porous MoO_2 was essentially grown on the internal surface of SBA-15 (Fig. S5†). The corresponding small-angle XRD patterns (Fig. S6†) suggest a consistent periodic mesostructure. Furthermore, from the high-resolution TEM image in Fig. 3b the interlamellar spacings can be estimated to be 0.34 nm which is consistent with MoO_2 (011). After hydrothermal treatment with TAA for 6 h, it can be seen that the MoO_2 surface was extensively roughened where the sheet-like structures were most likely MoS_2 (Fig. 3c). From Fig. 3d, two interlamellar spacings can be identified. One is 0.61 nm that might be ascribed to MoS_2 (002), consistent with the XRD results in Fig. 2a, and the other is 0.34 nm for MoO_2 (011). Interestingly, the MoS_2 nanosheets were mostly aligned perpendicular to the surface of one-dimensional MoO_2, exposing abundant folded edges that are known to exhibit high catalytic activity for HER.[29,30] Selected area electron diffraction studies were then carried out with a MoS_2/MoO_2-6 h bundle (Fig. 3e), and the patterns in Fig. 3f display concentric rings that might be assigned to MoS_2 (003), (101), and (113), and diffraction spots for MoO_2 (112) and (011), respectively, indicating that the prepared nanocomposites were indeed composed of monocrystalline MoO_2 and polycrystalline MoS_2.

XPS measurements were then carried out to further investigate the chemical composition and valence states of the samples, which are shown in Fig. 4. From the survey spectra in panel (a), the elements of Mo, S, O and C can be clearly identified. The C element shows a major peak at 284.5 eV that is characteristic of sp^2 C (Fig. 4b). Fig. 4c depicts the high-resolution scans of the Mo3d electrons with two major peaks at 229.6 eV and 232.8 eV, consistent with Mo $3d_{3/2}$ and $3d_{5/2}$ for MoO_2 and MoS_2, respectively.[19,31] The shoulder at 235.4 eV is likely due to the existence of a small amount of Mo^{6+}.[32–34] Meanwhile, the S2p electrons exhibited various bonding energies for S^{2-} (162.4 eV, 163.7 eV, 164.9 eV, and 226.9 eV), as shown in Fig. 4c and d.

The electrocatalytic activities for HER of the samples prepared above were then examined by electrochemical measurements in 0.5 M H_2SO_4. From Fig. 5a, it can be seen that MoO_2 exhibited poor catalytic activity for HER, with almost no reduction currents until the electrode potential was more negative than −0.4 V (black curve). In sharp contrast, apparent non-zero cathodic currents can be seen at the electrode modified by MoS_2/MoO_2-6 h (blue curve) with an onset potential of −0.104 V (*vs.* RHE) and a small Tafel slope of 76.1 mV dec^{-1} from Fig. 5b. Such a performance is markedly better than that of pure MoS_2 (red curve, −188 mV, 137.2 mV dec^{-1}) at the same catalyst loading. At the same overpotential (−0.3 V), the current density of the MoS_2/MoO_2-6 h electrode (−51.5 mA cm^{-2}) was about 11 times higher than that of pure MoS_2 (−4.7 mA cm^{-2}). In addition, one can see that the HER activity diminished somewhat with the prolonging hydrothermal reaction time (Fig. S7†), possibly because of increasing charge transfer resistance with an increasing coverage of MoS_2 that is less conductive than MoO_2 (Fig. S8†). Yet, one may notice that the activity remains subpar as compared to that of

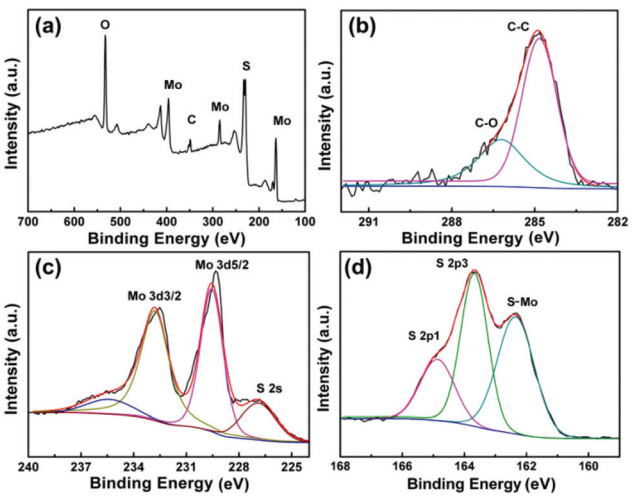

Fig. 4 (a) XPS survey spectra and high-resolution scans of (b) C 1s, (c) Mo 3d and (d) S 2p electrons of MoS_2/MoO_2-6 h. Black curves are experimental data and colored curves are deconvolution fits.

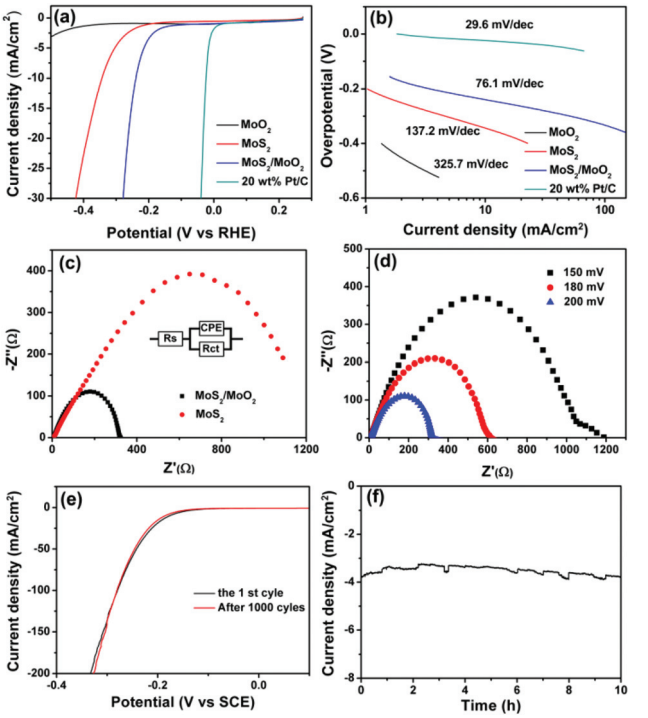

Fig. 5 (a) Polarization curves for HER in 0.5 M H_2SO_4 on a glassy carbon electrode modified with MoO_2, MoS_2, MoS_2/MoO_2-6 h and 20 wt% Pt/C, respectively. Potential sweep rate 5 mV s^{-1}. (b) Corresponding Tafel plots (overpotential *versus* log current density) derived from (a). (c) Nyquist plots and the equivalent circuit of MoS_2 and MoS_2/MoO_2-6 h at a potential of −200 mV (*vs.* RHE). (d) MoS_2/MoO_2-6 h at various HER overpotentials in 0.5 M H_2SO_4. (e) HER polarization curves for MoS_2/MoO_2-6 h before and after 1000 cycles of potential sweeps. (f) Current–time plots of the MoS_2/MoO_2-6 h electrode at an applied potential of −0.23 V (*vs.* RHE).

the commercial 20 wt% Pt/C catalysts (green curve, −0.01 V, 29.4 mV dec^{-1}).

Electrochemical impedance spectroscopy (EIS) is also a powerful technique in the characterization of interfacial reactions and electron-transfer kinetics in HER. Fig. 5c and d show the representative Nyquist plots of the MoS_2/MoO_2-6 h and MoS_2-modified glassy-carbon electrodes. More detailed analyses were carried out by fitting the impedance spectra to an equivalent circuit (Fig. 5c inset), where a constant phase element (CPE) was employed. The charge transfer resistance (R_{ct}) of the MoS_2/MoO_2-6 h electrode (148.5 Ω) was found to be markedly lower than that of the pure MoS_2 (661.2 Ω), suggesting that the highly conductive MoO_2 substrates reduced the resistance of the composite catalysts of MoS_2/MoO_2-6 h. In fact, from Fig. S9,† it can be seen that at a potential of −200 mV (*vs.* RHE), the series resistance (R_s) was reduced from 7.3 Ω for MoS_2 to 6.2 Ω for MoS_2/MoO_2-6 h. In addition, from Fig. 5d, it can be seen that R_{ct} of MoS_2/MoO_2-6 h decreased significantly with increasing overpotentials, from 503.2 Ω at −150 mV to 148.5 Ω at −200 mV, as evidenced by the apparent shrinkage of the diameter of the semicircles. In addition, R_{ct} was found to increase with the prolonging hydrothermal reaction time, suggesting that an increasing loading of MoS_2 nanosheets on the MoO_2 surface hindered charge transport (Fig. S8†).

In addition to good catalytic activity, the MoS_2/MoO_2 electrode also exhibited good stability for HER. Fig. 5e shows that, after 1000 potential cycles, the *J–V* curve of the MoS_2/MoO_2-6 h electrode remained almost unchanged. To further investigate the stability of MoS_2/MoO_2-6 h and MoO_2 in HER, the current–time plots at an applied potential of −0.23 V (*vs.* RHE) were collected and depicted in Fig. 5f and S10,† respectively. It can be seen that the reduction currents remained almost invariant over 10 h of continuous operation, indicating excellent durability of the electrodes for HER in 0.5 M H_2SO_4. These behaviors are actually very similar to that of commercial 20 wt% Pt/C (Fig. S11†).

Experimentally, a number of bubbles were observed on the surface of the MoS_2/MoO_2-6 h electrode (Fig. S12a†). The gas was confirmed to be hydrogen by gas chromatography measurements, and the rate of hydrogen production was estimated to be 120 mmol g^{-1} h^{-1}, as depicted in Fig. S12b.†

Such an HER performance of MoS_2/MoO_2 (onset overpotential −104 mV, Tafel slope 67.3 mV dec^{-1}) is better than or comparable to those of the leading Mo-based HER catalysts, such as semi-metallic MoS_2 ultrathin nanosheets (−130 mV, 69 mV dec^{-1}),[35] MoS_2 nanoflower-decorated reduced graphene oxide paper (−190 mV, 95 mV dec^{-1}),[36] and $MoSe_2$ nanosheets/graphene hybrids (−150 mV, 101 mV dec^{-1}),[37] but somewhat lower than that of WS_2 (−142 mV, 70 mV dec^{-1})[38] and MoS_x/NCNT (−75 mV, 40 mV dec^{-1}).[39] This may be attributed to the following factors. The first is the high electronic conductivity of MoO_2 (8.8×10^{-5} Ω cm at 300 K in bulk samples), as confirmed by electrochemical impedance spectroscopic measurements where the charge-transfer resistance of MoS_2/MoO_2 was markedly smaller than that of pure MoS_2 (Fig. 5c). Second, the continuously interconnected pore structures of MoO_2 provided effective channels for mass transport. Third, the vertically aligned MoS_2 nanosheets offered abundant edge sites, leading to fast interdomain electron transport and high HER activity.

Conclusion

In this study, porous metallic MoO_2-supported MoS_2 nanosheets (MoS_2/MoO_2) were prepared by sulfuration treatments of porous MoO_2 where the top layers of MoO_2 were hydrothermally transformed into MoS_2. One-dimensional porous MoO_2 was prepared by calcination of phosphomolybdic acid using mesoporous silica (SBA-15) as the template. The charge transfer resistance of the MoS_2/MoO_2 nanocomposites in HER was found to be markedly lower than that of pure MoS_2, most likely because the highly conductive MoO_2 significantly reduced the resistance of the composite catalyst. Electrochemical studies showed that the obtained electrocatalysts exhibited excellent HER activity with an onset potential of −104 mV (*vs.* RHE), a large current density (10 mA cm^{-2} at −0.24 V), a small Tafel slope of 76.1 mV dec^{-1} and robust electrochemical durability. The HER performance might be ascribed to the high electrical conductivity and porous structure of MoO_2 that allowed for effective charge and mass transport.

Acknowledgements

This work was supported by the National Recruitment Program of Global Experts, the PhD Start-up Funds of the Natural Science Foundation of Guangdong Province (S2013040016465), and Zhujiang New Stars of Science & Technology (2014J2200061).

Notes and references

1 E. Anxolabéhère-Mallart, C. Costentin, M. Fournier, S. Nowak, M. Robert and J.-M. Savéant, *J. Am. Chem. Soc.*, 2012, **134**, 6104–6107.
2 R. Subbaraman, D. Tripkovic, D. Strmcnik, K.-C. Chang, M. Uchimura, A. P. Paulikas, V. Stamenkovic and N. M. Markovic, *Science*, 2011, **334**, 1256–1260.
3 W. Zhou, X.-J. Wu, X. Cao, X. Huang, C. Tan, J. Tian, H. Liu, J. Wang and H. Zhang, *Energy Environ. Sci.*, 2013, **6**, 2921–2924.
4 J. D. Benck, T. R. Hellstern, J. Kibsgaard, P. Chakthranont and T. F. Jaramillo, *ACS Catal.*, 2014, **4**, 3957–3971.
5 C. He, X. Wu, J. Shen and P. K. Chu, *Nano Lett.*, 2012, **12**, 1545–1548.
6 M. L. Helm, M. P. Stewart, R. M. Bullock, M. R. DuBois and D. L. DuBois, *Science*, 2011, **333**, 863–866.
7 D. Gopalakrishnan, D. Damien and M. M. Shaijumon, *ACS Nano*, 2014, **8**, 5297–5303.

8 M. S. Faber and S. Jin, *Energy Environ. Sci.*, 2014, **7**, 3519–3542.
9 L. Cheng, W. Huang, Q. Gong, C. Liu, Z. Liu, Y. Li and H. Dai, *Angew. Chem., Int. Ed.*, 2014, **53**, 7860–7863.
10 Z. Xing, Q. Liu, A. M. Asiri and X. Sun, *Adv. Mater.*, 2014, **26**, 5702–5707.
11 W. Zhou, K. Zhou, D. Hou, X. Liu, G. Li, Y. Sang, H. Liu, L. Li and S. Chen, *ACS Appl. Mater. Interfaces*, 2014, **6**, 21534–21540.
12 D. V. Esposito, S. T. Hunt, A. L. Stottlemyer, K. D. Dobson, B. E. McCandless, R. W. Birkmire and J. G. Chen, *Angew. Chem., Int. Ed.*, 2010, **49**, 9859–9862.
13 B. Hinnemann, P. G. Moses, J. Bonde, K. P. Jørgensen, J. H. Nielsen, S. Horch, I. Chorkendorff and J. K. Nørskov, *J. Am. Chem. Soc.*, 2005, **127**, 5308–5309.
14 Y.-H. Chang, C.-T. Lin, T.-Y. Chen, C.-L. Hsu, Y.-H. Lee, W. Zhang, K.-H. Wei and L.-J. Li, *Adv. Mater.*, 2013, **25**, 755–755.
15 X. Ge, L. Chen, L. Zhang, Y. Wen, A. Hirata and M. Chen, *Adv. Mater.*, 2014, **26**, 3100–3104.
16 W. Zhou, Y. Zhou, L. Yang, J. Huang, Y. Ke, K. Zhou, L. Li and S. Chen, *J. Mater. Chem. A*, 2015, **3**, 1915–1919.
17 Y. Li, H. Wang, L. Xie, Y. Liang, G. Hong and H. Dai, *J. Am. Chem. Soc.*, 2011, **133**, 7296–7299.
18 J. Xie, J. Zhang, S. Li, F. Grote, X. Zhang, H. Zhang, R. Wang, Y. Lei, B. Pan and Y. Xie, *J. Am. Chem. Soc.*, 2013, **135**, 17881–17888.
19 W. Zhou, D. Hou, Y. Sang, S. Yao, J. Zhou, G. Li, L. Li, H. Liu and S. Chen, *J. Mater. Chem. A*, 2014, **2**, 11358–11364.
20 D. Kong, H. Wang, J. J. Cha, M. Pasta, K. J. Koski, J. Yao and Y. Cui, *Nano Lett.*, 2013, **13**, 1341–1347.
21 D. B. Rogers, R. D. Shannon, A. W. Sleight and J. L. Gillson, *Inorg. Chem.*, 1969, **8**, 841–849.
22 J. Xie, H. Zhang, S. Li, R. Wang, X. Sun, M. Zhou, J. Zhou, X. W. Lou and Y. Xie, *Adv. Mater.*, 2013, **25**, 5807–5813.
23 J. Liu, S. Tang, Y. Lu, G. Cai, S. Liang, W. Wang and X. Chen, *Energy Environ. Sci.*, 2013, **6**, 2691–2697.
24 Y. Shi, B. Guo, S. A. Corr, Q. Shi, Y.-S. Hu, K. R. Heier, L. Chen, R. Seshadri and G. D. Stucky, *Nano Lett.*, 2009, **9**, 4215–4220.
25 T.-W. Kim, F. Kleitz, B. Paul and R. Ryoo, *J. Am. Chem. Soc.*, 2005, **127**, 7601–7610.
26 M. Gong, Y. Li, H. Wang, Y. Liang, J. Z. Wu, J. Zhou, J. Wang, T. Regier, F. Wei and H. Dai, *J. Am. Chem. Soc.*, 2013, **135**, 8452–8455.
27 M. A. Lukowski, A. S. Daniel, F. Meng, A. Forticaux, L. Li and S. Jin, *J. Am. Chem. Soc.*, 2013, **135**, 10274–10277.
28 B. Windom, W. G. Sawyer and D. Hahn, *Tribol. Lett.*, 2011, **42**, 301–310.
29 D. Y. Chung, S.-K. Park, Y.-H. Chung, S.-H. Yu, D.-H. Lim, N. Jung, H. C. Ham, H.-Y. Park, Y. Piao, S. J. Yoo and Y.-E. Sung, *Nanoscale*, 2014, **6**, 2131–2136.
30 Y. Yan, X. Ge, Z. Liu, J.-Y. Wang, J.-M. Lee and X. Wang, *Nanoscale*, 2013, **5**, 7768–7771.
31 W. Zhou, Z. Yin, Y. Du, X. Huang, Z. Zeng, Z. Fan, H. Liu, J. Wang and H. Zhang, *Small*, 2013, **9**, 140–147.
32 J. D. Benck, Z. Chen, L. Y. Kuritzky, A. J. Forman and T. F. Jaramillo, *ACS Catal.*, 2012, **2**, 1916–1923.
33 L. Yuwen, F. Xu, B. Xue, Z. Luo, Q. Zhang, B. Bao, S. Su, L. Weng, W. Huang and L. Wang, *Nanoscale*, 2014, **6**, 5762–5769.
34 Z. Chen, D. Cummins, B. N. Reinecke, E. Clark, M. K. Sunkara and T. F. Jaramillo, *Nano Lett.*, 2011, **11**, 4168–4175.
35 X. Sun, J. Dai, Y. Guo, C. Wu, F. Hu, J. Zhao, X. Zeng and Y. Xie, *Nanoscale*, 2014, **6**, 8359–8367.
36 C.-B. Ma, X. Qi, B. Chen, S. Bao, Z. Yin, X.-J. Wu, Z. Luo, J. Wei, H.-L. Zhang and H. Zhang, *Nanoscale*, 2014, **6**, 5624–5629.
37 H. Tang, K. Dou, C.-C. Kaun, Q. Kuang and S. Yang, *J. Mater. Chem. A*, 2014, **2**, 360–364.
38 M. A. Lukowski, A. S. Daniel, C. R. English, F. Meng, A. Forticaux, R. J. Hamers and S. Jin, *Energy Environ. Sci.*, 2014, **7**, 2608–2613.
39 D. J. Li, U. N. Maiti, J. Lim, D. S. Choi, W. J. Lee, Y. Oh, G. Y. Lee and S. O. Kim, *Nano Lett.*, 2014, **14**, 1228–1233.